Sound Velocity Anisotropy and Single-Crystal Elastic Moduli of MgO to 43 GPa

Xinze Zhang, Chenhui Li, Feng Xu, Jinqiang Zhang, Chang Gao, Zhikang Cheng, Ye Wu, Xun Liu, Andreas Zerr, Haijun Huang

Sound velocity anisotropy and single-crystal elastic moduli of MgO to 43 GPa

Xinze Zhang[1], Chenhui Li[2], Feng Xu[1,*], Jinqiang Zhang[1], Chang Gao[1], Zhikang Cheng[1], Ye Wu[1], Xun Liu[1], Andreas Zerr[3,*], and Haijun Huang[1,*]

[1]School of Science, Wuhan University of Technology, 430070 Wuhan, China.
[2]State Key Laboratory of Superlattices and Microstructures, Institute of Semiconductors, Chinese Academy of Sciences, 100083 Beijing, China.
[3]Laboratoire des Sciences des Procédés et des Matériaux, CNRS UPR 3407, Université Sorbonne Paris Nord, 93430 Villetaneuse, France.

Key Points:

- Sound velocities along particular directions in MgO single crystals were measured to 43 GPa using time-domain Brillouin scattering.
- Upon compression, the Zener anisotropy ratio of MgO decreases steadily from above unity to below unity.
- The aggregate shear moduli of MgO and $(Mg_{1-x},Fe_x)O$ increase with pressure similarly but that of $(Mg_{1-x},Fe_x)O$ is smaller.

Abstract

Seismic anisotropy in the Earth's lower mantle likely results from a combination of elastic anisotropy and lattice preferred orientations of its main constituent minerals. As the second most abundant component of the lower mantle, ferropericlase has been widely studied, and the experimental results demonstrated, in general, a growing with pressure elastic anisotropy up to 1 Mbar. However, the unique measurements on the endmember (MgO) at comparable pressure conditions contradict the above observations and theoretical results. Here, time-domain Brillouin scattering was applied to measure longitudinal sound velocities in single crystals of MgO compressed in diamond anvil cell. Velocities along two particular crystallographic directions, [100] and [111], were independently collected to 43 GPa. Applying the known bulk modulus, a complete set of single-crystal elastic moduli, elastic anisotropy and aggregate shear modulus were derived. Our results revealed a steadily increasing with pressure elastic anisotropy at P > 20 GPa, consistent with the previous theoretical predictions and measurements on ferropericlase with moderate amounts of iron.

1. Introduction

Seismological observations revealed significant anisotropies at different depths of the Earth's lower mantle, including the uppermost (~660-1200 km) (Beghein and Trampert, 2004; Chang et al., 2014; Sturgeon et al., 2019) and the bottom (~2600-2900 km) (Lay and Helmberger, 1983; Lay et al., 1998) regions. These anisotropies are likely related to a combination of strong elastic anisotropy of minerals constituting the lower mantle and their preferred orientations caused by convection of the Earth's interior (Marquardt et al., 2009; McNamara et al., 2002; Romanowicz and Wenk, 2017; Wenk et al., 2006). Measurement of single-crystal elastic moduli, C_{ij}, of the main constituents of the lower mantle is thus necessary for establishing realistic models of the mantle dynamics. Ferropericlase, $(Mg_{1-x},Fe_x)O$ having rocksalt structure, is considered to be the second most abundant constituent of the lower mantle after Bridgmanite, $(Mg_{1-x},Fe_x)SiO_3$ with a low x having perovskite-type structure, or its high-pressure post-perovskite phase (Murakami et al., 2004; Oganov and Ono, 2004). According to the available experimental and computational studies, elastic anisotropy of highly compressed ferropericlase is significant (Wu et al., 2013; Yang et al., 2015) and stronger than that of Bridgmanite (Wentzcovitch et al., 2006). Because ferropericlase is mechanically weaker than Bridgmanite (Karato, 1989), it preferably accumulates the plastic deformation of the highly strained lower-mantle environment and thus develops stronger texture. For this reason, it has been proposed that preferred orientation in the textured ferropericlase could control the observed seismic anisotropy in the lower mantle (Marquardt et al., 2009).

Magnesium oxide (MgO) is the endmember of the $(Mg_{1-x},Fe_x)O$ family, commonly with $x \leq 0.2$, crystallizing in the same cubic B1 structure (space group $Fm\bar{3}m$) at pressures of the Earth's mantle (Duffy et al., 1995; Lee et al., 2004; Wu et al., 2013). Pressure dependence of single-crystal elastic moduli, $C_{ij}(P)$, of MgO is expected to be similar to that of $(Mg_{1-x},Fe_x)O$, except that the addition of iron causes anomaly around the pressure of the iron-related spin transition (Lin et al., 2005). In this limited pressure range, significant softening of elastic moduli of $(Mg_{1-x},Fe_x)O$ was reported (Antonangeli et al., 2011; Crowhurst et al., 2008; Marquardt et al., 2009; Wu et al., 2013; Yang et al., 2015). However, the expected similarity was not thoroughly elaborated, because much less experimental efforts were invested in the measurement of $C_{ij}(P)$ of MgO when compared to $(Mg_{1-x},Fe_x)O$. Besides, MgO was also proposed as a pressure gauge because of its compressibility and structural stability to extreme pressures of at least 228 GPa (Dorfman et al., 2012). For the same reason, MgO was also used as a standard solid for testing new theoretical methods aiming investigation of high-pressure and high-temperature elastic properties of minerals (Wu et al., 2011; Karki et al., 1997).

In general, sound velocity measurement along different crystallographic orientations in single crystals permits extraction of the complete set of C_{ij} values. At high pressures, conventional ultrasonic technique (frequencies in the MHz range) allows direct measurements of acoustic velocities via the pulse-echo method. Although the data accuracy can be guaranteed, relatively big sample sizes limit the accessible pressures to $P < 8$ GPa (Jackson and Nielsler, 1982; Yoneda, 1990). In contrast, Brillouin light scattering (BLS) is a versatile technique permitting measurement of sound velocities in transparent solids to much higher pressures: With adapted diamond anvil cell (DAC), BLS has been used to measure sound velocities in MgO single crystals up to 55 GPa (Fan et al., 2019; Sinogeikin and Bass, 2000; Zha et al., 2000). Recently, another promising technique, namely time-domain Brillouin scattering (TDBS) coupled with a DAC, was used to study $C_{ij}(P)$ of compressed transparent solids (Boccato et al., 2022; Gusev and Ruello, 2018; Kuriakose et al., 2017; Nikitin et al., 2015; Raetz et al., 2019). TDBS, also called picosecond laser ultrasonics (Thomsen et al., 1986); Zhao2019), can be considered as a combination of the advantages of the two abovementioned techniques: (i) it measures directly and in real time velocities of the stimulated coherent acoustic pulses, CAPs, which guarantees the signal quality (as in conventional ultrasonic technique), (ii) it is an all-optical method which allows measurements at pressures achievable in a DAC (as is the case for the BLS). The further advantage of the TDBS technique is a high axial resolution of the velocity measurements, better than 1 μm (Nikitin et al., 2015; Sandeep et al., 2021; Xu et al., 2021), not accessible for the conventional pulse-echo ultrasonics and for the BLS method. Power of the TDBS in high-pressure studies was already proved in earlier publications reporting extraction of complete sets of $C_{ij}(P)$ of cubic solids from polycrystalline sample (Kuriakose et al., 2017; Raetz et al., 2019; Xu et al., 2021; Xu et al., 2022).

In the present work, we used the TDBS to measure sound velocities in MgO but via a rather traditional way: In particular, we measured pressure dependences of velocities of longitudinal acoustic waves (LAW) in MgO single crystals, $V_{L[100]}$ and $V_{L[111]}$, along the particular crystallographic directions, [100] and [111]. Our choice was based on the well-known fact, also applied in the previous studies, that velocities of LAWs along these directions reach the extreme values in any cubic crystal including MgO (Karki et al., 1999; Kuriakose et al., 2017b; Raetz et al., 2019; Xu et al., 2021; Zha et al., 2000). Then, applying the previously measured equation of state (EOS), the complete set of $C_{ij}(P)$ of MgO was determined up to 43 GPa. Here, measurement of the LAW velocities along the third special direction in a cubic crystal, namely [110], was expendable because it is not an independent parameter and can be derived from the $V_{L[100]}$ and $V_{L[111]}$ (Xu et al., 2021).

2. Materials and Methods

2.1 Sample preparation and pressure generation

MgO single crystals in form of quadratic slices with sizes of 5×5×0.5 mm (from HF-Kejing, Ltd.) were used to prepare the samples. Normal directions to their larger surfaces were collinear with one of the two crystallographic directions, [100] or [111]. At ambient conditions, the cubic lattice parameter was measured to be 4.216 Å and the density calculated to be 3.58 g/cm^3. We deposited, on one side of each crystal, a thin film of tungsten (200-300 nm in thickness) via the magnetron sputtering. This film served as an opto-acoustic transducer in our TDBS experiments because the high acoustic impedance

of tungsten permitted generation of sufficiently strong CAPs and, accordingly, TDBS signals. Prior to loading in a DAC, velocities of the LAWs along the two directions, [100] and [111], were measured by the TDBS technique to be $V_{L[100]}$ = 9.09(17) km/s and $V_{L[111]}$ = 10.17(12) km/s, respectively, using the previously reported experimental refractive index at ambient pressure (Schifferle et al., 2022), see below for details. These values were in excellent agreement with those published in the literature (see Table 1). After that, each of the crystals was polished on the metal-free side to the thickness of about 20 μm and cleaved into smaller pieces. Those with perfect surface quality and with lateral dimensions optimal for the loading in a DAC were selected for the high-pressure experiments.

Table 1. $V_{L[100]}$ and $V_{L[111]}$ of MgO at ambient conditions. For the previous publications, the velocities were derived from the reported $C_{ij}(P)$ values.

Study	Method[a]	$V_{L[100]}$ (km/s)	$V_{L[111]}$ (km/s)
This study	TDBS	9.09(17)	10.17(12)
Jackson and Nielsler (1982)	UI	9.10	10.16
Yoneda et al. (1990)	UI	9.14	10.17
Sinogeikin and Bass (2000)	BLS	9.12(3)	10.14(4)
Zha et al. (2000)	BLS	9.10	10.16
Fan et al. (2019)	BLS	9.12(1)	10.12(1)
Karki et al. (1999)	DFT	8.79	9.81
Tsuchiya and Kawamura (2001)	DFT	9.22	10.06

The numbers in parentheses give uncertainties in the last significant digit.
[a]TDBS = time-domain Brillouin scattering; UI = ultrasonic interferometer; BLS = Brillouin light scattering; DFT = density functional theory.

High pressures were generated using a symmetric-type DAC equipped with beveled diamond anvils. Two experimental runs were performed. In the first run, a MgO crystal with the [100] orientation was examined using the diamond anvils with culets of 400 μm in diameter. A rhenium gasket was pre-indented to a thickness of 47 μm and a hole of 150 μm in diameter was drilled in the center. In the second run, we examined a MgO crystal with the [111] orientation. Here, we used diamond anvils with culets of 300 μm in diameter and a rhenium gasket of 38 μm in thickness and a hole of 100 μm in diameter. The hole in the gasket provided the sample volume which was first filled with NaCl powder and compressed until the whole volume became transparent. Then, the diamond anvil with the gasket sitting on it was lifted, and the sample with ruby grains was placed on the cleaned culet of the opposite anvil. After that, the sample sitting on the anvil culet was pressed in the NaCl which served as the pressure transmitting medium (PTM), see Figure 1. This loading method minimized local/non-uniform deformation of the sample upon further compression. NaCl was selected as the PTM because: (i) it possesses comparable yield strength as the typical gas-PTMs (such as solid helium, neon or argon) in the whole pressure range of our experiments (Mi et al., 2018); (ii) a moderate compressibility of NaCl ensured a considerable thickness of the sample chamber and, accordingly, moderate pressure gradients when compared with such noble-gas PTM such as helium (Xu et al., 2022); (iii) loading of a fluid PTM can easily cause lifting of the sample from the anvil culet, and thus change the sample orientation (Kuriakose et al., 2017a). Suitability of NaCl as a quasi-hydrostatic PTM is also supported by its application in the classical BLS measurements to pressures exceeding 100 GPa (Fei et al., 2007; Murakami et al., 2009). In each run, two ruby grains were placed around the sample and pressures were then determined, for each of them, from the calibrated shift of the ruby R1 fluorescence line (Dewaele et al., 2008). The sample pressure was derived from the average for the two grains.

2.2 Time-domain Brillouin scattering

A schematic representation of our TDBS set-up based on a femtosecond pulsed laser is shown in Figure 1. In detail, we used a mode-locked Ti:sapphire laser (Chameleon Ultra, Coherent) generating light pulses with the wavelength of λ = 800 nm, repetition rate of 80 MHz and pulse width of 140 fs. The laser radiation was split into a pump and a probe beams which were used to generate ultrashort CAPs and to follow their propagation, respectively. The pump laser pulses were modulated by an

acousto-optic modulator at 1 MHz to insure synchronous detection of the TDBS signals. To exclude contribution of scattered radiation of the pump beam to the collected signals, a two-color scheme was used: The photon frequency of the pump beam was doubled with a nonlinear beta-barium borate crystal which resulted in the wavelength decrease to λ = 400 nm. The probe laser pulses passed through a mechanically controlled delay line permitting a continuous change of the delay time from 0 to 8 ns with respect to the pump pulses. Then, both the pump and probe beams were focused onto the sample through an objective with magnification of ×50 and a long working distance of 20 mm adapted to the geometry of our DAC. The synchronous detection was finally performed to extract the modulated component from the total radiation reflected and scattered from all optical elements and interfaces, including the diamond anvils and the sample.

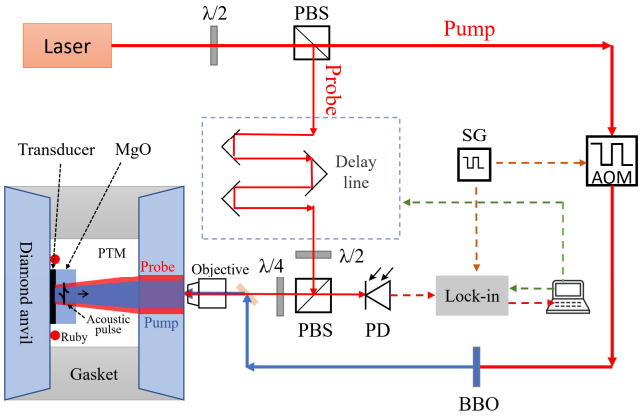

Figure 1. Schematics of our TDBS set-up. PBS: polarizing beam splitter, AOM: acousto-optic modulator, SG: signal generator providing the 1 MHz square-wave signals to the AOM and to the lock-in amplifier, BBO: beta-barium borate crystal, PD: photoelectric detector. At the bottom left, a magnified schematic of the sample in the DAC is shown together with the paths of the focused pump and probe laser beams and the generated CAP scattering a part of the probe beam.

The TDBS measurements were performed in the reflection geometry where both pump and probe beams were focused on the same side of the sample (Figure 1). CAPs were generated at the interface of the transducer and the MgO crystal and propagated inside the MgO crystal towards the MgO/NaCl interface, parallel to the DAC axis. This geometry was applied because it guaranteed the maximal amplitude of the CAPs propagating in the MgO samples and, accordingly, the strongest TDBS signals. In a transmission geometry, where the pump beam is focused on the opposite side of the transducer, e.g. the diamond/transducer interface, the CAP would be attenuated during its propagation through the transducer and reflection at the transducer/MgO interface. A typical TDBS signal collected in the reflection geometry is shown in Figure 2a. A sudden jump of a few ps duration, caused by the coincidence of the pump and probe pulses, is followed by a sluggish decay (hundreds of ps, in our case) of the signal intensity. Here, the continuous thermal background due to the dissipation of heat from the irradiated area is superimposed with oscillations, called Brillouin oscillations (Figure 2b). They result from the interference of the probe pulse intensity scattered by the propagating CAP and reflected by stationary interfaces in the sample and outside (e.g. diamond/air interface). A detailed description of the TDBS technique can be found elsewhere (Decremps et al., 2015; Nikitin et al., 2015). For our experimental geometry, where the CAPs and the probe beam propagated collinearly, the oscillation frequency (f_B) is proportional to the acoustic wave velocity (V_i) according to the following equation (Sandeep et al., 2021; Thomsen et al., 1986; Xu et al., 2013):

$$f_B = \frac{2nV_i}{\lambda} \quad (1)$$

where λ is wavelength of the probe beam in vacuum (800 nm in this work), n is refractive index of the sample material at the same wavelength, and i stands for the acoustic wave type (L for LAW or T for transversal acoustic waves - TAW). It should be noted that LAWs with corresponding frequencies f_B were always detected in the collected TDBS signals. These f_B values were used to derive $V_{L[100]}$ or

$V_{L[111]}$ and then $C_{ij}(P)$ of MgO. Figure 2 shows an example of the TDBS signal obtained for the [111]-oriented sample of MgO at P = 15.2 GPa. Even though this is not the "best" one (e.g. with just one oscillation frequency as in the most cases) we showed it due to the potential presence of an additional frequency component, which could be attributed to a TAW mode. In order to follow evolution of this signal along the CAP path, we performed a short-time Fourier transform (STFT) analysis of the oscillations (Figure 2b) using a temporal window of ~2 oscillations subsequently shifted along the pump-probe delay times. Unfortunately, we could not recognize the TAW mode at any step but just the LAW mode. Apparently, the contribution of the TAW mode in the short window was below the detection level. Also, the LAW-mode frequencies were found to scatter between 45.3 and 46.6 GHz which is consistent with the FWHM of the peak (δf_B = 1.5 GHz, Figure 2c) obtained from the fast Fourier transformation (FFT) over the entire delay-time duration. Thus, our experimental uncertainties in the presented below LAW velocities $V_{L[100]}$ and $V_{L[111]}$ were extracted from the FWHM of the obtained FFT peaks.

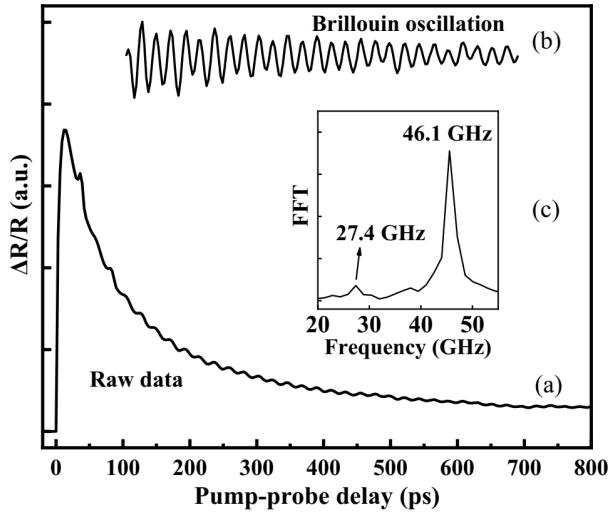

Figure 2. Typical TDBS signal recorded for the [111]-oriented sample of MgO at P = 15.2 GPa and its treatment. (a) The raw signal shows a relative change of the sample transient reflectivity as a function of the pump-probe delay time. (b) Brillouin oscillations obtained after the subtraction of the thermal background from the raw signal. Amplitude of the oscillations was magnified for better visibility. (c) Fourier transformation of the signal in (b) revealed a strong peak at f_B = 46.1(7) GHz corresponding to the LAW, and a weak peak at f_B=27.4(5) GHz which could be attributed to the TAW.

It should be noted that our MgO samples remained single crystals in the whole pressure range of our experiments for two reasons: (i) The axially resolved f_B values along the sample axis (i.e. the propagating trajectory of the CAP inside the crystal) were constant up to the longest delay time of the collected signals (e.g. Figure 2b). If a part of a crystal cracked and rotated, we would observe a change in the local f_B value due to the elastic anisotropy of MgO and, accordingly, different V_L. (ii) Comparison of the yield strengths of the sample, MgO, and the pressure medium, NaCl, indicates elastic deformation of the MgO crystals and plastic deformation of NaCl, as should be for any PTM: The yield strength of MgO at atmospheric pressure of σ_y ~ 1.5 GPa strongly exceeds that of NaCl of σ_y ~ 0.08 GPa (Weidner et al., 1994). Upon compression, σ_y of MgO steadily increases to 4 GPa at P = 40 GPa (Meade and Jeanloz, 1988) while σ_y of NaCl remains below 1 GPa (Mi et al., 2018). Thus, the uniaxial stress developing in NaCl under compression, limited by its σ_y, is insufficient to induce any plastic deformation in our MgO single crystals.

2.3 Refractive index

Because pressure dependence of refractive index, $n(P)$, of MgO at λ = 800 nm was not established, we used the recently published experimental values at λ = 600 nm (Schifferle et al., 2022), available at 1 atm. and at high pressures from 20 GPa to 140 GPa. For the values between 1 atm. and 20 GPa, we performed a back-extrapolation from the high to atmospheric pressure using a 2nd-order polynomial (see inset in Figure 3), and the extrapolated value at 1 atm. agreed perfectly with that directly

measured in the same work. For comparison, we also calculated $n(P)$ of MgO at λ = 800 nm using the density functional theory (DFT) for pressures between 1 atm. and 50 GPa. The calculations were performed using the projector augmented wave method (Blöchl, 1994) and a plane wave basis set, as implemented in the Vienna Ab-initio Simulation Package (VASP) (Kresse and Furthmüller, 1996). We chose the Perdew-Burke-Ernzerhof (PBE) functional (Perdew et al., 1996) within the generalized gradient approximation (GGA) to approximate the electron exchange-correlation interaction. The primitive unit cell of MgO containing two atoms was used in our DFT calculations. By setting a plane wave cutoff at 520 eV and applying a Γ-centered k-meshes grid of 20×20×20 in the first Brillouin-zone for integration, a total energy convergence of 5 meV/atom was reached. Below, both the calculated here and the above discussed experimental $n(P)$ were applied in order to derive $V_L(P)$ of MgO from the $f_B(P)$ dependences measured for each of the directions, [100] and [111].

3. Results and Discussion

3.1 Longitudinal sound velocities

Figure 3 presents our experimental $V_{L[100]}(P)$ and $V_{L[111]}(P)$, compared with the previously published results. MgO is known to exhibit considerable elastic anisotropy at atmospheric pressure where the fastest and the slowest crystallographic directions are [111] and [100], respectively. In this case, the Zener anisotropy ratio exceeds unity, $A = C_{44}/C' = 2C_{44}/(C_{11}-C_{12}) > 1$. However, $V_{L[100]}(P)$ increases with compression significantly faster than $V_{L[111]}(P)$ and meets the latter at $P \sim 20$ GPa. At this particular pressure, MgO is elastically isotropic. Upon further compression, the anisotropy emerges again but its character changes to the inverse: $V_{L[100]}(P)$ becomes higher than $V_{L[111]}(P)$ and $A < 1$.

In Figure 3, we present two sets of $V_{L[100]}(P)$ and $V_{L[111]}(P)$ obtained using either the recently measured $n(P)$ (Schifferle et al., 2022) or our calculated $n(P)$. In the former case, our experimental velocities (red triangles in Figure 3) agree well with all earlier measurements at pressures below ~20 GPa. Above ~20 GPa, our $V_{L[100]}(P)$ increases steadily till P = 43 GPa, in agreement with all theoretical predictions (Karki et al., 1999; Tsuchiya and Kawamura, 2001), but deviates from the earlier unique experimental result obtained using the BLS technique (Zha et al., 2000). In that work, $V_{L[100]}(P)$ flattens out and tends to cross $V_{L[111]}(P)$ another time at $P \sim 55$ GPa. In contrast, our $V_{L[111]}(P)$ agrees with the previous BLS data within the experimental uncertainties.

The dependences $V_{L[100]}(P)$ and $V_{L[111]}(P)$ we obtained using our calculated $n(P)$ (pink triangles in Figure 3) agree with other experimental results at atmospheric pressure and below ~10 GPa. At higher pressures, both $V_{L[100]}(P)$ and $V_{L[111]}(P)$ increase faster than those derived using the experimental $n(P)$. Obviously, this difference follows from the much faster decrease of our theoretical $n(P)$ with pressure (see inset in Figure 3). According to our DFT calculations, the difference in n for the wavelengths between 600 nm and 800 nm is very small both at atmospheric and high pressures, which is consistent with the experimental investigations (Schifferle et al., 2022; Stephens et al., 1952). Thus, the significant difference between the two sets of $n(P)$ is not due to the different wavelengths, but due to the different methods: measurements and DFT calculations. As shown in Figure 3, all calculated $n(P)$ show a steeper decrease with pressure when compared with the experimental ones, at least at $P > 20$ GPa where experimental data are available.

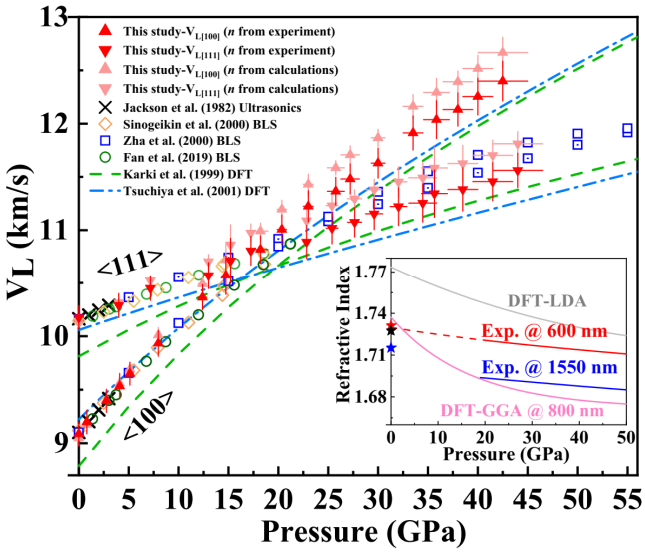

Figure 3. $V_{L[100]}$ and $V_{L[111]}$ of MgO as a function of pressure. Solid triangles showing up and down represent our measured $V_{L[100]}(P)$ and $V_{L[111]}(P)$, respectively, together with the experimental uncertainties. The pressure uncertainties correspond to the difference between the two ruby grains. The velocity uncertainties were determined from the accuracy of our measured $f_B(P)$, given by the FWHM of the FFT peak, and of the experimental $n(P)$. Here, the red and pink triangles show the velocities derived using the experimental $n(P)$ (Schifferle et al., 2022) and our calculated $n(P)$, respectively. Earlier experimental and computational results are shown as follows: ultrasonics – black crosses (Jackson and Nielsler, 1982); BLS – open orange diamonds (Sinogeikin and Bass, 2000), blue squares (open and with a dot inside) (Zha et al., 2000) and green circles (Fan et al., 2019); DFT calculations - green dashed (Karki et al., 1999) and blue dash-dotted (Tsuchiya and Kawamura, 2001) lines. Inset: refractive index of MgO as a function of pressure. Red line – recent measurements at λ = 600 nm under static compression (Schifferle et al., 2022), the dashed line represents the back extrapolation to low pressures. Red, black and blue stars – measurements at atmospheric pressure for λ = 600 nm (Schifferle et al., 2022), 800 nm and 1550 nm (Stephens and Malitson, 1952), respectively. Blue line – measurement under shock compression at λ = 1550 nm (Fratanduono et al., 2013). Gray and pink lines – previous (Oganov et al., 2003) and our present calculations using DFT approaches.

As mentioned above, the main discrepancy between our experimental results and those of Zha et al. (2000) is the different values of $V_{L[100]}$ at P > 20 GPa, which causes the corresponding differences in the derived elastic moduli C_{11} and C_{12} (see below). This discrepancy we attribute to an unfavorable position of the BLS peaks of MgO in the BLS measurements of Zha et al. (2000) overlapping, at higher pressures, with the peaks of the helium PTM which had to be subtracted. Unfortunately, the spectrum-treatment details (e.g. the measured BLS-peaks of pure helium PTM, used in the subtraction, compared with the original superposing BLS-peaks) were not presented in that paper. Also, the BLS peak of the longitudinal mode of MgO was shown to overlap with BLS peaks of diamond at pressures above ~30 GPa (Zha et al., 2000; Yang et al., 2016). Moreover, the three peaks shown in the work of Zha et al., 2000) were located at the high-frequency end of the BLS spectrum where their shapes were distorted by a very strong and steep background due to the Rayleigh peak. Because the frequency region was cut just after the diamond peak, a precise approximation of the Rayleigh peak intensity and, accordingly, correction of the BLS-peak of MgO could be problematic.

3.2 Single-crystal elastic moduli

As for any cubic crystal, the complete stiffness tensor of MgO has only three independent components, $C_{11}(P)$, $C_{12}(P)$, and $C_{44}(P)$, which can be derived from our experimental $V_{L[100]}(P)$ and $V_{L[111]}(P)$ if combined with the earlier measured pressure dependences of density, $\rho(P)$, and of the bulk modulus, $K(P)$. The C_{ij} of a cubic solid are related to the above parameters according to the following equations:

$$V_{L[100]} = \sqrt{\frac{C_{11}}{\rho}}, V_{L[111]} = \sqrt{\frac{C_{11}+2C_{12}+4C_{44}}{3\rho}} \quad (2)$$

$$K = \frac{C_{11}+2C_{12}}{3} \quad (3)$$

To treat our data, we used $\rho(P)$ and $K(P)$ measured by Speziale et al. (2001). The $C_{ij}(P)$ were derived for the both sets of $V_{L[100]}(P)$ and $V_{L[111]}(P)$ obtained using either the experimental or calculated $n(P)$ (Figure 4). For the sake of clarity, we focus below on the values derived using the experimental $n(P)$ (red triangles in Figure 4). We have found that $C_{11}(P)$ increases almost linearly with pressure, in good agreement with all earlier experiments performed at P < 20 GPa. It is also similar to the theoretical dependences in the whole pressure range. However, the previous experimental $C_{11}(P)$, obtained using the BLS technique, deviates significantly from our data at P > 20 GPa, as is the case for the corresponding LAW velocity, $V_{L[100]}(P)$, in Figure 3. Accordingly, our $C_{12}(P)$ also increases almost linearly with pressure, in contrast to the earlier experiments at P > 10 GPa, and its slope is similar to those predicted by Karki et al. (1999) and Tsuchiya et al. (2001). On the other hand, our and previous experimental $C_{44}(P)$ agree well with each other. In order to be able to derive elastic anisotropy $A(P)$ and the aggregate shear modulus $G(P)$ of MgO combining our data for $C_{11}(P)$ and $C_{12}(P)$ with those for $C_{44}(P)$, we fitted the latter three sets of data-points by 2nd order polynomials to $C_{ij}^{*}(P)$. Results of the least-square fits are summarized in Table 2.

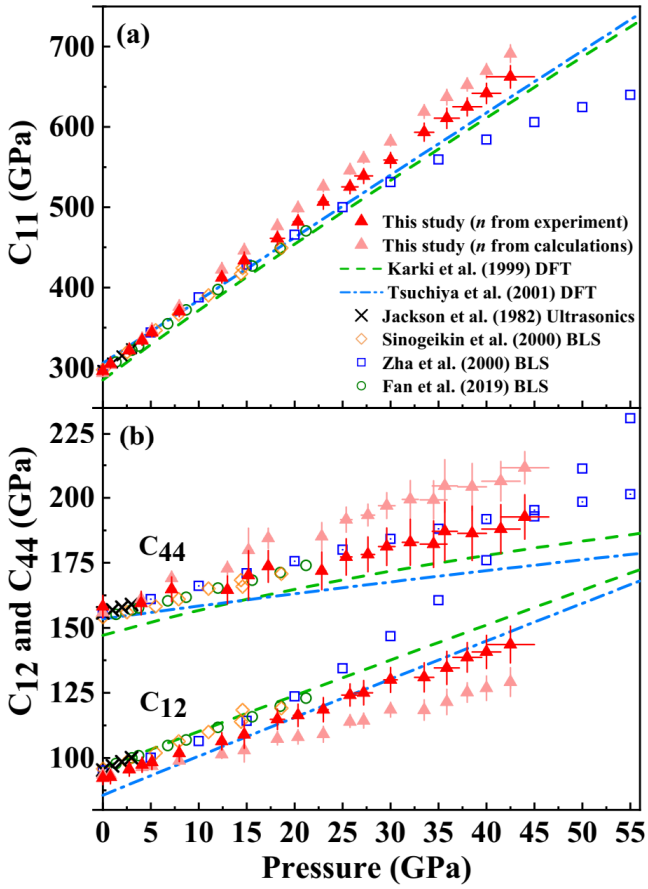

Figure 4. Pressure dependences of single-crystal elastic moduli, $C_{ij}(P)$, of MgO. The solid red and pink triangles with error bars are our experimental data-points obtained using the recently measured $n(P)$ (Schifferle et al., 2022), and our calculated $n(P)$, respectively. All previous results are presented in the same style as in Figure 3.

Table 2. Results of the least-square fits of quadratic polynomials $C_{ij}^{*}(P) = A_{ij} + B_{ij}P + D_{ij}P^2$ to our experimental data-points for MgO, obtained using the experimental $n(P)$

	A_{ij}	B_{ij}	D_{ij}
C_{11}^{*}, GPa	296.1(9)	9.55(11)	-0.023(3)
C_{12}^{*}, GPa	92.1(4)	1.19(5)	0.001(1)
C_{44}^{*}, GPa	157.9(14)	0.73(14)	0.001(3)

3.3 Elastic Anisotropy

Elastic anisotropy of cubic crystals can be quantified using the Zener ratio $A = C_{44}/C' = 2C_{44}/(C_{11}-C_{12})$ where $A = 1$ indicates the elastic isotropy. Our complete set of $C_{ij}(P)$ was obtained in two independent experimental runs for two crystal orientations, and the pressure values were different in each of the runs. For this reason, $A(P)$ was derived using the fitted 2nd order polynomials $C_{ij}^{*}(P)$ given in Table 2. The obtained $A(P)$ was found to decrease from 1.56 to 1 when pressure increases from 1 atm. to 18 GPa (Figure 5). Above 18 GPa, $A(P)$ decreases steadily from 1 to 0.73, indicating a continuous enhancement of elastic anisotropy of the inverse type, with $A(P) < 1$. Our pressure dependence of $A(P)$ is in good agreement with the earlier DFT calculations and disproves the earlier experiments of Zha et al. (2000) who reported a weak anisotropy up to $P = 55$ GPa. It should be noted here that choice of the refractive index does not significantly influence the recovered elastic anisotropy, as follows from the relation we derived from Equations 1, 2, and 3:

$$A = \frac{2C_{44}}{C_{11}-C_{12}} = \frac{\rho f_{B[111]}^2 \lambda^2 - 4n^2 K}{\rho f_{B[100]}^2 \lambda^2 - 4n^2 K} \quad (4)$$

For example, if n is underestimated by 1% in the pressure region where $A > 1$, V_L will be overestimated by 1% (see Equation 1) but the value of A will be underestimated by less than 0.5%. This weak dependence of elastic anisotropy on the chosen refractive index is confirmed by a close similarity of our dependences $A(P)$ derived using the earlier experimental (Schifferle et al., 2022) and our computational $n(P)$ (Figure 5).

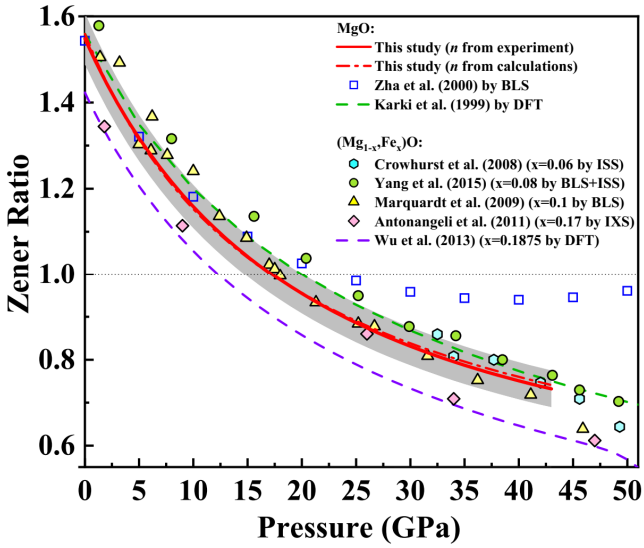

Figure 5. Zener anisotropy ratio A of MgO and HS-ferropericlase as a function of pressure. Our results for MgO are shown by solid and dash-dotted red lines derived from both experimental and computational $n(P)$, gray bands represent our experimental uncertainties for the dependence derived using the experimental $n(P)$. Blue open squares and green dashed line represent the earlier experimental (Zha et al., 2000) and computational (Karki et al., 1999) results for MgO, respectively. Solid hexagons (Crowhurst et al., 2008), circles (Yang et al., 2015), triangles (Marquardt et al., 2009) and diamonds (Antonangeli et al., 2011) are the earlier experimental $A(P)$ for $(Mg_{1-x},Fe_x)O$ with different degrees of iron substitution (x = 0.06 ~ 0.17), obtained using various experimental techniques. Purple dashed line represents computational results for $(Mg_{1-x},Fe_x)O$ with x = 0.1875 (Wu et al., 2013).

In Figure 5, the obtained here and the earlier $A(P)$ of MgO are compared with the earlier experimental and computational results for $(Mg_{1-x},Fe_x)O$ with various degrees of the substitution of Mg by Fe (Antonangeli et al., 2011; Crowhurst et al., 2008; Marquardt et al., 2009; Wu et al., 2013; Yang et al., 2015). The latter works reported that the presence of iron in $(Mg_{1-x},Fe_x)O$ causes a high- to the low spin transition (HS and LS) in the pressure range between ~40 and ~60 GPa (Lin et al., 2005) accompanied by an anomalous elasticity behavior. Because our present experiments were limited to P = 43 GPa, we compared our and earlier dependences for MgO with those for the HS-ferropericlase. The comparison shows that our pressure dependence of the Zener ratio of MgO at $P > 15$ GPa is, in

general, similar to that of HS-ferropericlase. This is in contrast to the previous unique BLS-data of Zha et al. (2000). On the other hand, the available experimental data do not reveal systematic dependence of $A(P)$ on the iron contents which could be anticipated if the computational dependences for MgO (Karki et al., 1999) and for $(Mg_{1-x},Fe_x)O$ with x=0.1875 (Wu et al., 2013) are compared. It appears to be premature to propose an explanation of the difference between the DFT calculations and the experiments because the experimental dependences were obtained using the principally different techniques. Further experiments on $(Mg_{1-x},Fe_x)O$ samples with different iron contents but applying one and the same technique, e.g. TDBS, could help to clarify the controversy.

3.4 Aggregate shear modulus

Figure 6 compares our aggregate shear modulus $G(P)$ of MgO with the earlier experimental and computational results. All values in the figure were calculated using the provided $C_{ij}(P)$ values applying the Hill approximation (Hill, 1952). At low pressures, our $G(P)$ derived using both the experimental and computational $n(P)$ agree well with that of Zha et al. (2000) but exceeds significantly the theoretical prediction (Karki et al., 1999). Upon further compression, both our $G(P)$ dependences increase monotonically with pressure, consistent with the previous measurements on polycrystalline MgO sample (Murakami et al., 2009), and with a recent study using neural networks involving all previous referenced data (Rijal et al., 2023). However, all of them are contrary to that of Zha et al. (2000) demonstrating flattening of $G(P)$ with increasing pressure. Our $G(P)$ derived using the calculated $n(P)$ grows faster with compression than that obtained using the experimental $n(P)$. The slope of $G(P)$ of $(Mg_{1-x},Fe_x)O$ with any x is similar to that of our $G(P)$ of MgO obtained using the experimental $n(P)$. Similarly to the above considered elastic anisotropy, computational results anticipated $G(P)$ decreasing with increasing iron content, but the experimental results do not reveal any systematic behavior.

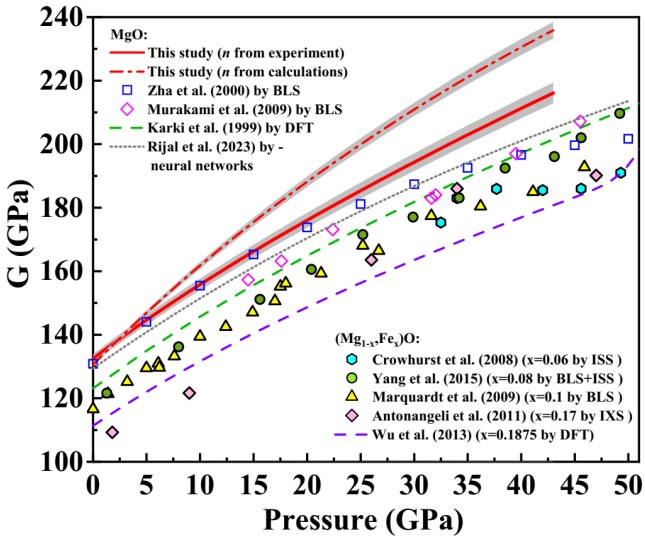

Figure 6. Aggregate shear modulus $G(P)$ of MgO and HS-ferropericlase as a function of pressure. Our results for MgO are shown by solid and dash-dotted red lines and the gray bands represent the experimental uncertainties. Previous BLS data for polycrystalline MgO are shown by open magenta diamonds (Murakami et al., 2009). A recent result obtained using neural networks is plotted by dotted gray line (Rijal et al., 2023). All other data are presented in the same style as in Figure 5.

4. Conclusions

In this work, we applied the TDBS technique to measure longitudinal sound velocities in single crystals of MgO compressed in a DAC to $P = 43$ GPa. In particular, the velocities were measured along two crystallographic directions in an MgO single crystal, [100] and [111]. Applying the measured $V_{L[100]}(P)$, $V_{L[111]}(P)$, and the previously published equation of state, we derived the complete set of single crystal elastic moduli $C_{ij}(P)$, then determined elastic anisotropy $A(P)$ and aggregate shear modulus $G(P)$ of MgO. In contrast to the unique earlier measurements to a similar degree of compression (Zha et al., 2000), we observed a steady increasing elastic anisotropy and aggregate shear

modulus of MgO at pressures of the lower mantle. This agrees with the previous DFT calculations and the measurements on $(Mg_{1-x},Fe_x)O$ thus strengthening the hypothesis that texturing and elastic anisotropy of ferropericlase can be at the origin of the seismic anisotropy in the lower mantle. Finally, we have demonstrated that the here applied advanced experimental technique of TDBS is highly suitable for the measurement of elastic properties of minerals at pressures and, eventually, temperatures of the Earth's mantle.

Acknowledgements
The authors acknowledge financial support from ZBYY-80922010601, NSFC-42274124, NSFC-41504070, CSC-201606955092. We sincerely thank Laurent Belliard and Bernard Perrin for technical support. We are grateful to Xing Liu and Zhihong Chen for preparation of the samples.

Data Availability Statement
The primary and processed data that support the findings of this study are available with the link: https://datadryad.org/stash/share/jF21IZ05TAX7cXGFGBbPK0VIk83LlB4WcHjHIySEsbs

References

Antonangeli, D., Siebert, J., Aracne, C. M., Farber, D. L., Bosak, A., Hoesch, M., Krisch, M., Ryerson, F. J., Fiquet, G., & Badro, J. (2011). Spin Crossover in Ferropericlase at High Pressure: A Seismologically Transparent Transition?, *Science*, *331*(6013), 64-67. https://doi.org/10.1126/science.1198429

Beghein, C., & Trampert, J. (2004). Probability density functions for radial anisotropy: implications for the upper 1200 km of the mantle, *Earth and Planetary Science Letters*, *217*(1), 151-162. https://doi.org/10.1016/S0012-821X(03)00575-2

Blöchl, P. E. (1994). Projector augmented-wave method, *Physical Review B*, *50*(24), 17953-17979. https://doi.org/10.1103/PhysRevB.50.17953

Boccato, S., et al. (2022). Picosecond acoustics: a new way to access elastic properties of materials at pressure and temperature conditions of planetary interiors, *Physics and Chemistry of Minerals*, *49*(6), 20. https://doi.org/10.1007/s00269-022-01194-6

Chang, S. J., Ferreira, A. M. G., Ritsema, J., van Heijst, H. J., & Woodhouse, J. H. (2014). Global radially anisotropic mantle structure from multiple datasets: A review, current challenges, and outlook, *Tectonophysics*, *617*, 1-19. https://doi.org/10.1016/j.tecto.2014.01.033

Crowhurst, J. C., Brown, J. M., Goncharov, A. F., & Jacobsen, S. D. (2008). Elasticity of (Mg,Fe)O through the spin transition of iron in the lower mantle, *Science*, *319*(5862), 451-453. https://doi.org/10.1126/science.1149606

Decremps, F., Gauthier, M., Ayrinhac, S., Bove, L., Belliard, L., Perrin, B., Morand, M., Le Marchand, G., Bergame, F., & Philippe, J. (2015). Picosecond acoustics method for measuring the thermodynamical properties of solids and liquids at high pressure and high temperature, *Ultrasonics*, *56*, 129-140. https://doi.org/10.1016/j.ultras.2014.04.011

Dewaele, A., Torrent, M., Loubeyre, P., & Mezouar, M. (2008). Compression curves of transition metals in the Mbar range: Experiments and projector augmented-wave calculations, *Physical Review B*, *78*(10), 104102. 10.1103/PhysRevB.78.104102

Dorfman, S. M., Prakapenka, V. B., Meng, Y., & Duffy, T. S. (2012). Intercomparison of pressure standards (Au, Pt, Mo, MgO, NaCl and Ne) to 2.5 Mbar, *Journal of Geophysical Research, Solid Earth*, *117*(B8). https://doi.org/10.1029/2012JB009292

Duffy, T. S., Hemley, R. J., & Mao, H.-K. (1995). Equation of state and shear strength at multimegabar pressures: Magnesium oxide to 227 GPa, *Physical Review Letters*, *74*(8), 1371-1374. https://doi.org/10.1103/PhysRevLett.74.1371

Fan, D., Fu, S., Yang, J., Tkachev, S. N., Prakapenka, V. B., & Lin, J.-F. (2019). Elasticity of single-crystal periclase at high pressure and temperature: The effect of iron on the elasticity and seismic parameters of ferropericlase in the lower mantle, *American Mineralogist*, *104*(2), 262-275. https://doi.org/10.2138/am-2019-6656

Fei, Y. W., Ricolleau, A., Frank, M., Mibe, K., Shen, G. Y., & Prakapenka, V. (2007). Toward an internally consistent pressure scale, Proceedings of the National Academy of Sciences of the United

States of America, 104(22), 9182-9186. https://doi.org/10.1073/pnas.0609013104
Fratanduono, D. E., Eggert, J. H., Akin, M. C., Chau, R., & Holmes, N. C. (2013). A novel approach to Hugoniot measurements utilizing transparent crystals, *Journal of Applied Physics*, *114*(4), 043518. https://doi.org/10.1063/1.4813871
Gusev, V. E., & Ruello, P. (2018). Advances in applications of time-domain Brillouin scattering for nanoscale imaging, *Applied Physics Reviews*, *5*(3), 20. https://doi.org/10.1063/1.5017241
Hill, R. (1952). The Elastic Behaviour of a Crystalline Aggregate, *Proceedings of the Physical Society. Section A*, *65*(5), 349-354. https://doi.org/10.1088/0370-1298/65/5/307
Jackson, I., & Nielsler, H. (1982), *The elasticity of periclase to 3 GPa and some geophysical implications*, Center for Academic Publications Japan, Tokyo.
Karato, S.-i. (1989). Plasticity-crystal structure systematics in dense oxides and its implications for the creep strength of the Earth's deep interior: a preliminary result, *Physics of the Earth and Planetary Interiors*, *55*(3), 234-240. https://doi.org/10.1016/0031-9201(89)90071-X
Karki, B. B., Wentzcovitch, R. M., de Gironcoli, S., & Baroni, S. (1999). First-principles determination of elastic anisotropy and wave velocities of MgO at lower mantle conditions, *Science*, *286*(5445), 1705-1707. https://doi.org/10.1126/science.286.5445.1705
Karki, B. B., Stixrude, L., Clark, S. J., Warren, M. C., Ackland, G. J., & Crain, J. (1997). Structure and elasticity of MgO at high pressure, *American Mineralogist*, *82*(1-2), 51-60. https://doi.org/10.2138/am-1997-1-207
Kresse, G., & Furthmüller, J. (1996). Efficient iterative schemes for ab initio total-energy calculations using a plane-wave basis set, *Physical Review B*, *54*(16), 11169-11186. https://doi.org/10.1103/PhysRevB.54.11169
Kuriakose, M., et al. (2017a). Longitudinal sound velocities, elastic anisotropy, and phase transition of high-pressure cubic H2O ice to 82 GPa, *Physical Review B*, *96*(13), 13. https://doi.org/10.1103/PhysRevB.96.134122
Kuriakose, M., et al. (2017b). Longitudinal sound velocities, elastic anisotropy, and phase transition of high-pressure cubic H2O ice to 82 GPa, Physical Review B, 96(13), 134122. https://doi.org/10.1103/PhysRevB.96.134122
Lay, T., & Helmberger, D. V. (1983). The shear-wave velocity gradient at the base of the mantle, *Journal of Geophysical Research: Solid Earth*, *88*(B10), 8160-8170. https://doi.org/10.1029/JB088iB10p08160
Lay, T., Williams, Q., & Garnero, E. J. (1998). The core–mantle boundary layer and deep Earth dynamics, *Nature*, *392*(6675), 461-468. https://doi.org/10.1038/33083
Lee, K. K. M., O'Neill, B., Panero, W. R., Shim, S.-H., Benedetti, L. R., & Jeanloz, R. (2004). Equations of state of the high-pressure phases of a natural peridotite and implications for the Earth's lower mantle, *Earth and Planetary Science Letters*, *223*(3), 381-393. https://doi.org/10.1016/j.epsl.2004.04.033
Lin, J.-F., Struzhkin, V. V., Jacobsen, S. D., Hu, M. Y., Chow, P., Kung, J., Liu, H., Mao, H.-k., & Hemley, R. J. (2005). Spin transition of iron in magnesiowüstite in the Earth's lower mantle, *Nature*, *436*(7049), 377-380. 10.1038/nature03825
Marquardt, H., Speziale, S., Reichmann, H. J., Frost, D. J., Schilling, F. R., & Garnero, E. J. (2009). Elastic Shear Anisotropy of Ferropericlase in Earth's Lower Mantle, *Science*, *324*(5924), 224-226. https://doi.org/10.1126/science.1169365
McNamara, A. K., van Keken, P. E., & Karato, S.-I. (2002). Development of anisotropic structure in the Earth's lower mantle by solid-state convection, *Nature*, *416*(6878), 310-314. https://doi.org/10.1038/416310a
Meade, C., & Jeanloz, R. (1988). Yield strength of MgO to 40 GPa, *Journal of Geophysical Research: Solid Earth*, *93*(B4), 3261-3269. https://doi.org/10.1029/JB093iB04p03261
Mi, Z., Shieh, S. R., Kavner, A., Kiefer, B., Wenk, H. R., & Duffy, T. S. (2018). Strength and texture of sodium chloride to 56 GPa, *Journal of Applied Physics*, *123*(13), 8. https://doi.org/10.1063/1.5022273
Murakami, M., Ohishi, Y., Hirao, N., & Hirose, K. (2009). Elasticity of MgO to 130 GPa: Implications for lower mantle mineralogy, Earth and Planetary Science Letters, 277(1-2), 123-129. https://doi.org/10.1016/j.epsl.2008.10.010
Murakami, M., Hirose, K., Kawamura, K., Sata, N., & Ohishi, Y. (2004). Post-Perovskite Phase

Transition in MgSiO3, *Science*, *304*(5672), 855-858. https://doi.org/10.1126/science.1095932
Nikitin, S. M., Chigarev, N., Tournat, V., Bulou, A., Gasteau, D., Castagnede, B., Zerr, A., & Gusev, V. E. (2015). Revealing sub-pm and pm-scale textures in H2O ice at megabar pressures by time-domain Brillouin scattering, *Scientific Reports*, *5*, 11. https://doi.org/10.1038/srep09352
Oganov, A. R., & Ono, S. (2004). Theoretical and experimental evidence for a post-perovskite phase of MgSiO3 in Earth's D" layer, *Nature*, *430*(6998), 445-448. https://doi.org/10.1038/nature02701
Oganov, A. R., Gillan, M. J., & Price, G. D. (2003). Ab initio lattice dynamics and structural stability of MgO, *Journal of Chemical Physics*, *118*(22), 10174-10182. https://doi.org/10.1063/1.1570394
Perdew, J. P., Burke, K., & Ernzerhof, M. (1996). Generalized Gradient Approximation Made Simple, *Physical Review Letters*, *77*, 3865. https://doi.org/10.1103/PhysRevLett.77.3865
Raetz, S., Kuriakose, M., Djemia, P., Nikitin, S. M., Chigarev, N., Tournat, V., Bulou, A., Lomonosov, A., Gusev, V. E., & Zerr, A. (2019). Elastic anisotropy and single-crystal moduli of solid argon up to 64 GPa from time-domain Brillouin scattering, *Physical Review B*, *99*(22), 10. https://doi.org/10.1103/PhysRevB.99.224102
Rijal, A., Cobden, L., Trampert, J., Marquardt, H., & Jackson, J. M. (2023). Shear properties of MgO inferred using neural networks, European Journal of Mineralogy, 35(1), 45-58. 10.5194/ejm-35-45-2023
Romanowicz, B., & Wenk, H. R. (2017). Anisotropy in the deep Earth, *Physics of the Earth and Planetary Interiors*, *269*, 58-90. https://doi.org/10.1016/j.pepi.2017.05.005
Sandeep, S., Threard, T., Savi, E. D., Chigarev, N., Bulou, A., Tournat, V., Zerr, A., Gusev, V. E., & Raetz, S. (2021). 3D characterization of individual grains of coexisting high-pressure H2O ice phases by time-domain Brillouin scattering, *Journal of Applied Physics*, *130*(5), 16. https://doi.org/10.1063/5.0056814
Schifferle, L., Speziale, S., & Lobanov, S. S. (2022). High-pressure evolution of the refractive index of MgO up to 140 GPa, *Journal of Applied Physics*, *132*(12), 125903. https://doi.org/10.1063/5.0106626
Sinogeikin, S. V., & Bass, J. D. (2000). Single-crystal elasticity of pyrope and MgO to 20 GPa by Brillouin scattering in the diamond cell, *Physics of the Earth and Planetary Interiors*, *120*(1-2), 43-62. https://doi.org/10.1016/s0031-9201(00)00143-6
Speziale, S., Zha, C.-S., Duffy, T. S., Hemley, R. J., & Mao, H.-k. (2001). Quasi-hydrostatic compression of magnesium oxide to 52 GPa: Implications for the pressure-volume-temperature equation of state, Journal of Geophysical Research: Solid Earth, 106(B1), 515-528. https://doi.org/10.1029/2000JB900318
Stephens, R. E., & Malitson, I. H. (1952). Index of Refraction of Magnesium Oxide, *Journal of Research of the National Bureau of Standards*, *49*(4), 249-252. https://doi.org/10.6028/jres.049.025
Sturgeon, W., Ferreira, A. M. G., Faccenda, M., Chang, S. J., & Schardong, L. (2019). On the Origin of Radial Anisotropy Near Subducted Slabs in the Midmantle, *Geochemistry Geophysics Geosystems*, *20*(11), 5105-5125. https://doi.org/10.1029/2019gc008462
Thomsen, C., Grahn, H. T., Maris, H. J., & Tauc, J. (1986). Surface generation and detection of phonons by picosecond light pulses, *Physical Review B*, *34*(6), 4129-4138. https://doi.org/10.1103/PhysRevB.34.4129
Tsuchiya, T., & Kawamura, K. (2001). Systematics of elasticity: Ab initio study in B1-type alkaline earth oxides, *Journal of Chemical Physics*, *114*(22), 10086-10093. https://doi.org/10.1063/1.1371498
Weidner, D. J., Wang, Y., & Vaughan, M. T. (1994). Yield strength at high pressure and temperature, *Geophysical Research Letters*, *21*(9), 753-756. https://doi.org/10.1029/93GL03549
Wenk, H. R., Speziale, S., McNamara, A. K., & Garnero, E. J. (2006). Modeling lower mantle anisotropy development in a subducting slab, *Earth and Planetary Science Letters*, *245*(1), 302-314. https://doi.org/10.1016/j.epsl.2006.02.028
Wentzcovitch, R. M., Tsuchiya, T., & Tsuchiya, J. (2006). MgSiO3 postperovskite at D" conditions, *Proceedings of the National Academy of Sciences of the United States of America*, *103*(3), 543-546. https://doi.org/10.1073/pnas.0506879103
Wu, Z. Q., & Wentzcovitch, R. M. (2011). Quasiharmonic thermal elasticity of crystals: An analytical approach, Physical Review B, 83(18), 184115. 10.1103/PhysRevB.83.184115
Wu, Z. Q., Justo, J. F., & Wentzcovitch, R. M. (2013). Elastic Anomalies in a Spin-Crossover System:

Ferropericlase at Lower Mantle Conditions, *Physical Review Letters*, *110*(22), 5. https://doi.org/10.1103/PhysRevLett.110.228501

Xu, F., Djemia, P., Belliard, L., Huang, H. J., Perrin, B., & Zerr, A. (2021). Influence of elastic anisotropy on measured sound velocities and elastic moduli of polycrystalline cubic solids, *Journal of Applied Physics*, *130*(3), 10. https://doi.org/10.1063/5.0053372

Xu, F., Belliard, L., Fournier, D., Charron, E., Duquesne, J. Y., Martin, S., Secouard, C., & Perrin, B. (2013). Complete elastic characterization of lithium phosphorous oxynitride films using picosecond ultrasonics, Thin Solid Films, 548, 366-370. https://doi.org/10.1016/j.tsf.2013.08.080

Xu, F., Belliard, L., Li, C., Djemia, P., Becerra, L., Huang, H., Perrin, B., & Zerr, A. (2022). Single-crystal elastic moduli, anisotropy and the B1-B2 phase transition of NaCl at high pressures: Experiment vs. ab-initio calculations. arXiv:2209.10899

Yang, J., Tong, X. Y., Lin, J. F., Okuchi, T., & Tomioka, N. (2015). Elasticity of Ferropericlase across the Spin Crossover in the Earth's Lower Mantle, *Scientific Reports*, *5*, 9. https://doi.org/10.1038/srep17188

Yang, J., Lin, J.-F., Jacobsen, S. D., Seymour, N. M., Tkachev, S. N., & Prakapenka, V. B. (2016). Elasticity of ferropericlase and seismic heterogeneity in the Earth's lower mantle, *Journal of Geophysical Research: Solid Earth*, 121(12), 8488-8500. https://doi.org/10.1002/2016JB013352

Yoneda, A. (1990). Pressure Derivatives of Elastic Constants of Single Crystal MgO and MgAl2O4, *Journal of Physics of the Earth*, *38*(1), 19-55. https://doi.org/10.4294/jpe1952.38.19

Zha, C.-S., Mao, H.-k., & Hemley, R. J. (2000). Elasticity of MgO and a primary pressure scale to 55 GPa, *Proceedings of the National Academy of Sciences of the United States of America*, *97*(25), 13494-13499. https://doi.org/10.1073/pnas.240466697

Zhao, B., Xu, F., Belliard, L., Huang, H. J., Perrin, B., Djemia, P., & Zerr, A. (2019). Sound Velocities and Elastic Moduli of Phases I and V of Silicon at High Pressures, *Physica Status Solidi Rapid Research Letters*, *13*(8), 4. https://doi.org/10.1002/pssr.201900173